Electronic Supplementary Information

Crystalline phase effects of zirconia in Ag/ZrO_2 catalyst: oxygen vacancy-mediated new pathways to promote carbon-oxygen bonds hydrogenation

Menghan Guo[1], Xiaofang Shang[1], Jiawei Li, Chenxi Yang, Jie Ding*, Qin Zhong*, Yixin Chen

School of Chemistry and Chemical Engineering, Nanjing University of Science and Technology, Nanjing, Jiangsu Province, 210094, PR China

* Corresponding author. E-mail address: zq304@njust.edu.cn (Q. Zhong), tonlyjding@njust.edu.cn (J. Ding).

[1] These authors contributed equally to this work and should be considered co-first authors.

Catalytic characterisation

The X-ray diffraction (XRD) patterns of the samples were obtained using a D2 PHASER (Bruker, Germany) equipped with Cu Kα radiation. The data were collected at 5°-80° with a step size of 0.01°.

The nitrogen adsorption-desorption isotherm was determined utilising an automatic aperture analyser (Micromeritics, ASAP 2460). Prior to the commencement of the test, all samples were subjected to a drying process at 120 °C for a period of 24 h and a degassing process at 300 °C for a further 6 h. The total specific surface area (S_{BET}) was determined by a multipoint BET method. The single-point pore volume was estimated from the amount adsorbed at a relative pressure of 0.99.

The morphology was investigated using field emission scanning transmission microscopy (SEM, Regulus-8100, HITACHI, Japan) and transmission electron microscopy (TEM, HT-7800, HITACHI, Japan).

The surface chemical environments of the samples were determined by X-ray photoelectron spectroscopy (XPS, AXIS ULTRA DLD, Shimadzu, Japan) with Al Kα radiation (hν = 1486.6 eV), and all the data were corrected by the C 1s adventitious located at 284.4 eV.

Fourier-transform infrared (FTIR) spectra were recorded in the 4000-400 cm^{-1} range on a Thermo fisher Nicolet iS10 spectrometer equipped with a deuterated tri-glycine sulfate (DTGS) detector with fast recovery. The powder samples were mixed with KBr (2 wt.%) and pressed into translucent disks at room temperature.

The UV-vis diffuse reflectance spectra (UV-vis DRS) was characterised through a Shimadzu UV-2600 UV-vis spectrophotometer, with a test range of 800-220 nm.

The thermal decomposition products of the samples were analysed using a TPR-20 EGA (Hiden Analytical) mass spectrometer in multi-ion detection mode.

Electron paramagnetic resonance spectroscopy (EPR, Bruker) is employed to quantify single-electron structures, including free radicals, transition metal ions, polymorphic molecules, and crystal defects, among others, in samples.

Thermogravimetric curves were obtained for the samples on a thermogravimetric analyser (SDT Q600, Simultaneous DSC-TGA Q Series, TA Instruments-Waters LLC, USA). Given that the mass of the sample remains relatively constant, the derivative of the mass taken in the vertical coordinate is employed to enhance the results. The mass of all the samples tested was taken as 3 mg.

In-situ FTIR experiments

In-situ Fourier transform infrared spectroscopy (in-situ FTIR) of DEO was performed on a Thermo fisher Nicolet iS10 spectrometer equipped with a liquid-nitrogen-cooled mercury cadmium telluride (MCT) narrow-

band detector and a modified In-situ reaction cell. The spectra were recorded in a cumulative manner, with 32 scans at a resolution of 4 cm^{-1}.

The detailed pre-treatment and test conditions are given as follows. Firstly, about 100 mg of sample was carefully put onto the support copper net of reaction cell. Afterwards, the sample was pre-reduced in a N_2 flow (30 $mL \cdot min^{-1}$) at 300 °C with a heating rate of 10 $°C \cdot min^{-1}$ for 2 h. In this process, the background spectrum was collected. Subsequently, the line was switched, with the DEO liquid in the bubbler bottle being carried by N_2 into the reaction cell. FTIR spectra were collected at 10 min intervals over a period of 2 h.

H_2-TPR experiments

Hydrogen temperature-programmed reduction (H_2-TPR) was conducted on an automated catalyst characterisation system (Micromeritics, AutoChem II 2920, America) equipped with a TCD detector.

In a typical experiment, 100 mg of the ground sample was added to the tube via a long-necked funnel. The sample (100 mg) was subjected to a pretreatment at 120 °C (Ag_2O decomposes spontaneously at high temperatures) for one hour in an argon atmosphere (50 $mL \cdot min^{-1}$), after which it was cooled to 50 °C. Subsequently, the carrier gas was replaced with a 10 vol.% H_2/Ar mixture at a flow rate of 50 $mL \cdot min^{-1}$. The sample was then heated to 800 °C at a rate of 10 $°C \cdot min^{-1}$, and the TCD signals were recorded. The water and carbon dioxide generated during the experiment were removed by means of a 5A molecular sieve.

DFT calculation

First-principle theoretical calculations at the density functional theory (DFT) level are conducted. Spin-polarized DFT calculations are performed utilizing the Vienna Ab-initio Simulation Package (VASP, Version 5.4.4) [1] The Perdew-Burke-Ernzerhof (PBE) functional within the generalized gradient approximation (GGA) [2, 3] is utilized to describe electronic exchange and correlation. To rectify the self-interaction error of GGA, Hubbard U corrections (DFT+U) approach is employed with the U_{eff} = 2 eV to the Zr 4d orbitals according to the previous studies [4]. The cell model ZrO_2 is downloaded from materials project (mp-2858, a = 5.234 Å, b = 5.269 Å, c = 5.418 Å, $\alpha = \gamma = 90$ º, $\beta = 100$ º, space group = $P2_1/c$). For the cell parameter optimization, the interaction between core and electrons is described using the projector-augmented wave approach with cut-off energy of 450 eV. The van-der Waals interactions are corrected by the Grimme's DFT-D3 method [5]. A 4×4×4 Monkhorst-Pack (M-P) k-point grid is used to optimize cell parameters and static analysis. All the spin-polarized calculation is conducted with magnetic moment parameters.

By cleaving the (-111) facet of optimized ZrO_2 cell, a 3×2×1 supercell model is constructed (a = 20.313 Å, b = 14.718 Å, c = 20.695 Å, $\alpha = \beta = 90$ º, $\gamma = 64$ º). The construction of ZrO_2 models with oxygen vacancies

involved the removal of bridging oxygen or tridentate oxygen on the slab model, resulting in two structural ZrO_2 models with oxygen vacancies. A 1×2×1 k-point mesh centered around the gamma point is conducted to optimize the slab model. To prevent interactions between different models along the Z-axis, a vacuum layer with a thickness of 15 Å is implemented. In these surface models, the bottom periodic layer is fixed to maintain the bulk structure, while all other atoms are allowed to fully relax. Atomic structures are optimized with the electronic and ionic relaxation thresholds set at 10^{-5} eV and 20 meV·$Å^{-1}$, respectively. Fig. S1 shows the cell with fully optimized parameters, and the cell parameter was fully optimized.

The adsorption energy (E_{ads}) of DEO on ZrO_2 were calculated as follows:

$$E_{ads} = E_{DEO\text{-}slab} - E_{DEO} - E_{slab}$$

Where, $E_{DEO\text{-}slab}$, E_{DEO} and E_{slab} are total energy for the slab model of ZrO_2 with DEO, the optimized DEO model and the slab model of ZrO_2.

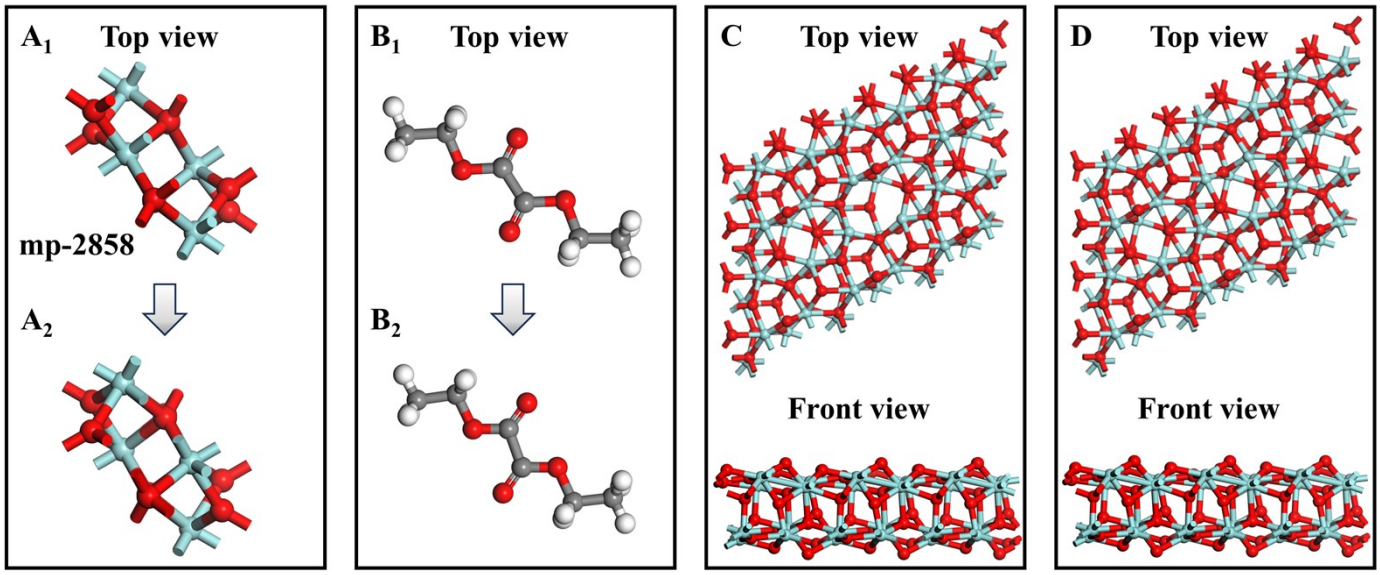

Fig. S1. (A_1) Cell model of ZrO_2 and (A_2) the optimized model of ZrO_2. (B_1) The initial DEO model and (B_2) the optimized DEO module. The slab model of ZrO_2 with (C) tridentate bridging oxygen vacancies and (D) bridging oxygen vacancies (3×2×1 supercell model). The colors of the atoms are designated as follows: O (red), Zr (cyan), C (dark grey) and H (white).

Supplementary Figures

Table S1 abbreviation-full name comparison table

Abbreviation	Full name or details
DEO	Diethyl oxalate
EGly	Ethyl glycolate
EG	Ethylene glycol
LHSV	Liquid hourly space velocity
A/B	A load on B, A is usually a metal, B is a support
Zr-NH_4^+	Monoclinic phase zirconia prepared with ammonium carbonate as precipitant
Zr-Na^+	Tetragonal phase zirconia prepared with sodium carbonate as precipitant
Zr-Na^+/NH_4^+-X00	X00 stands for calcination temperature
O_v	Oxygen vacancy
Zr^{n+}	n takes values of 3 or 4, representing different coordination environments of Zr
v_{as}	Symmetrical stretching vibration
v_s	Asymmetric stretching vibration
δ_{as}	Asymmetrical deformation vibration

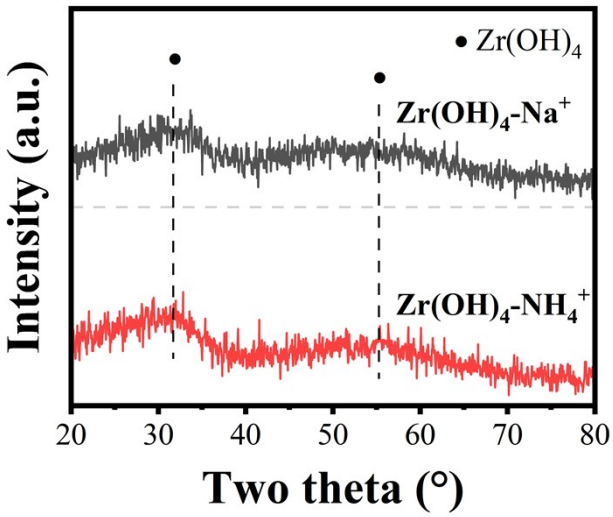

Fig. S2. XRD patterns of precursors.

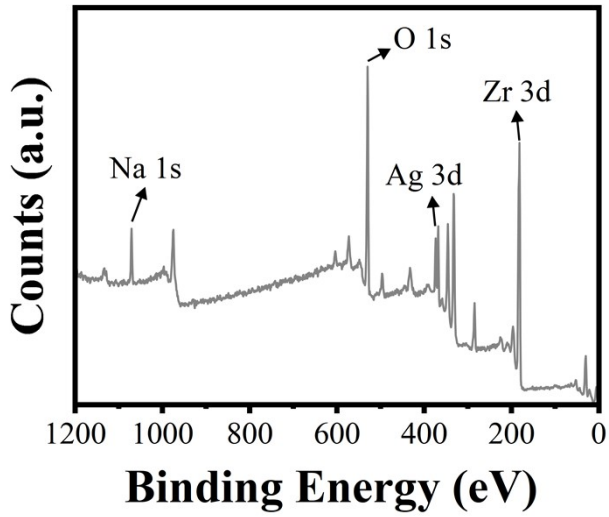

Fig. S3. The full XPS spectra of Zr-Na^+ catalyst.

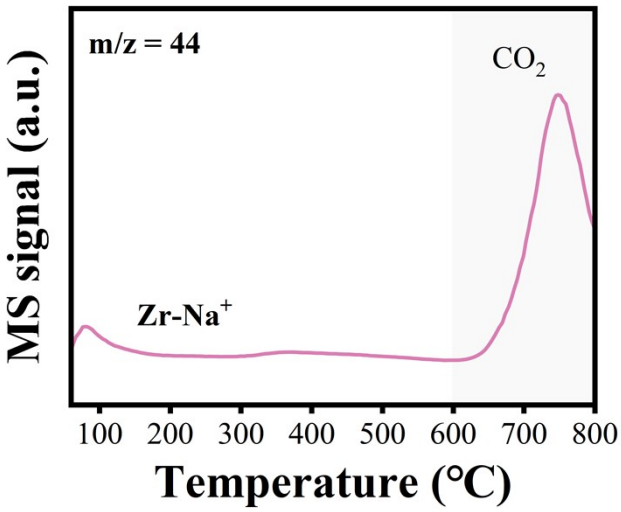

Fig. S4. The MS profiles of Zr-Na^+ catalyst in an atmosphere of helium.

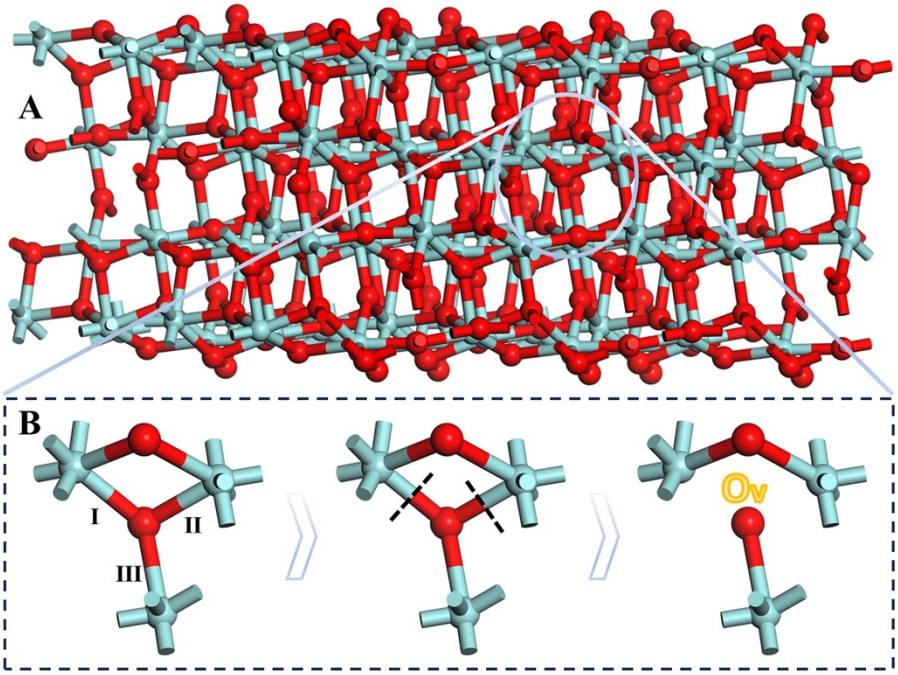

Fig. S5. (A) Crystallite structure of (-111) crystalline plane of the monoclinic zirconia. (B) One possible pathway for the formation of Zr^{3+}-O_v cite (red for oxygen, cyan for zirconium).

The representative bulk-phase three-coordinated oxygen in Fig. S5A was selected as the object of study, as illustrated in Fig. S5B. With regard to the oxygen atom in question, it can be observed that the chemical environments of all three Zr-O bonds are distinct, and that they are designated as I, II and III, respectively. If the Zr-O bond (III) is retained while the Zr-O bond (I) and Zr-O bond (II) are broken during the phase transformation, an oxygen vacancy accompanied by Zr^{3+} is generated after separation because the Zr-O bond (I) and Zr-O bond (II) are still bridged by an oxygen atom.

This process represents a reasonable hypothesis regarding the experimental results, which require further investigation and discussion.

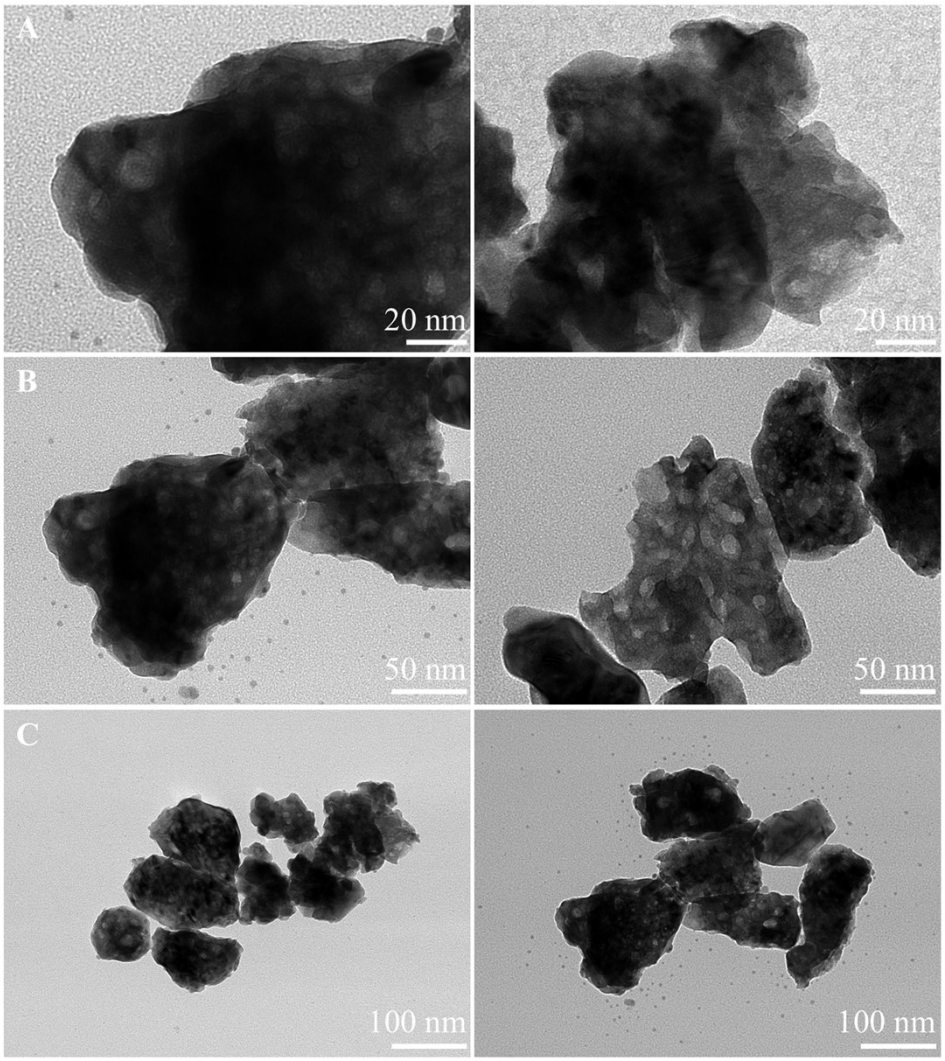

Fig. S6. TEM images of Zr-Na^+ catalyst at (A) 20 nm, (B) 50 nm and (C) 100 nm.

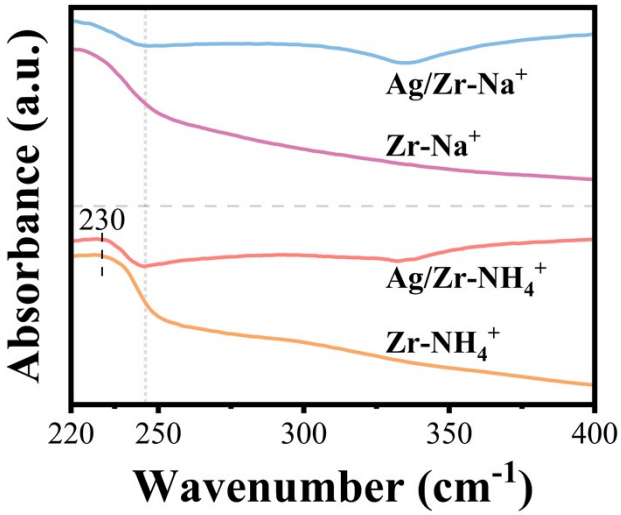

Fig. S7. UV-vis DRS spectra of Zr-Na^+, Zr-NH_4^+, Ag/Zr-Na^+ and Ag/Zr-NH_4^+ catalysts

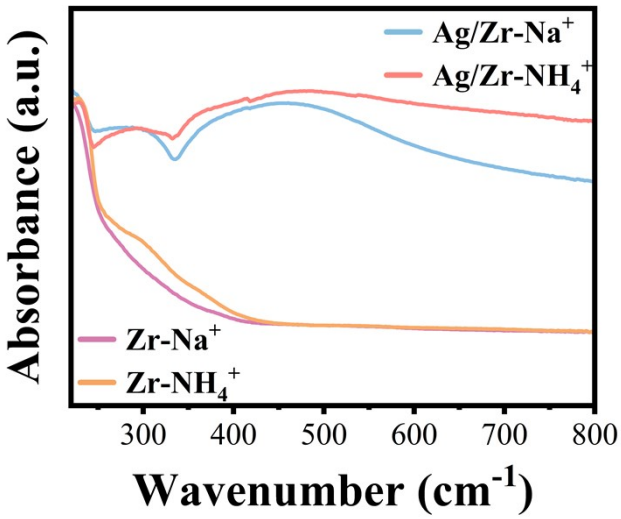

Fig. S8. UV-vis DRS spectra of different materials at the same coordinate origin.

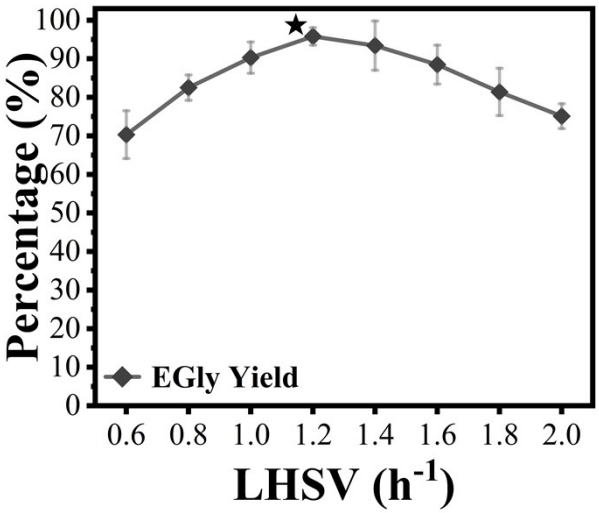

Fig. S9. Effect of LHSV on the EGly yield of Ag/Zr-NH_4^+ catalyst.

Table S2 Comparison of the activity performance of silver-based catalysts

Catalyst	Con./%	Sel./%	Yield/%	P/MPa	T/°C	H_2/DM(E)O	(W)LHSV/h^{-1}	Lifetime/h	Ref.
DMO hydrogenation to MG									
15Ag/SiO_2	100	92	92	2.5	220	100	0.2	120	[6]
10Ag/MCM-41	-	-	90	2.5	220	100	0.2	-	[7]
10Ag/SBA-15	99.5	95	94.5	3	200	100	0.6	100	[8]
5Ag_1-$Ni_{0.20}$/SBA-15	97.6	92.8	90.6	3	200	80	1	140	[9]
10Ag-in/hCNT	100	97	97	3	220	80	0.6	200	[10]
15Ag/KCC-1	97.8	92.2	90.2	3	200	100	1.75	110	[11]
10Ag/AC-N	100	95	95	3	220	80	0.6	150	[12]
10%Ag/SiO_2	86.8	91.5	79.4	1.5	220	150	0.28	150	[13]
10Ag/0.02Ti-KCC-1	98	95	93	3	200	100	1.75	100	[14]
3Ag/NH_2-MSNS	100	96.6	96.6	2	220	100	1	250	[15]
5Ag1–$Li_{0.05}$/SBA-15	99.45	82.2	81.75	3	200	80	0.6	200	[16]
3Ag/MSNS_90	99.7	96.6	96.3	2	220	80	1.25	100	[17]
1B/Ag/SiO_2	100	88.3	88.3	1.5	220	150	0.28	300	[18]
10Ag-0.5%Ni/SiO_2	100	92.5	92.5	1.5	220	150	0.28	300	[19]
10Ag/m-ZrO_2	-	-	98.8	3	205	80	0.6	1000	[20]
DEO hydrogenation to EGly									
30Ag-HMO	90	82	73.8	2.9	240	-	-	200	[21]
10Ag/SiO_2-HR	95.6	82.9	79.2	1.5	160	200	0.2	100	[22]
5Ag/Zr-NH_4^+	99.9	95.9	95.8	2	220	100	0.5	120	This work

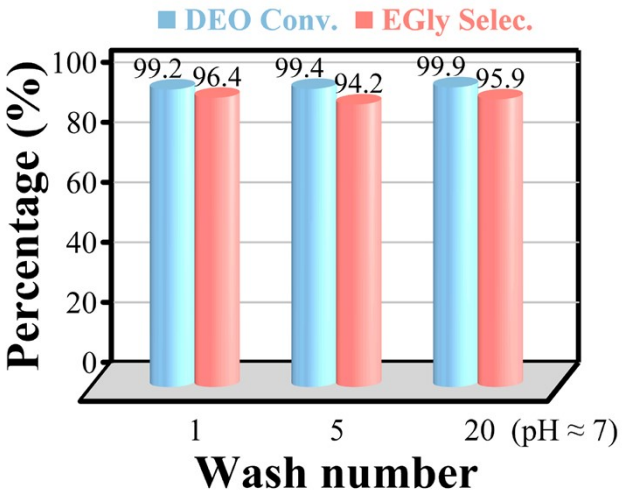

Fig. S10. Effect of wash number on the activity of Ag/Zr-Na^+ catalyst.

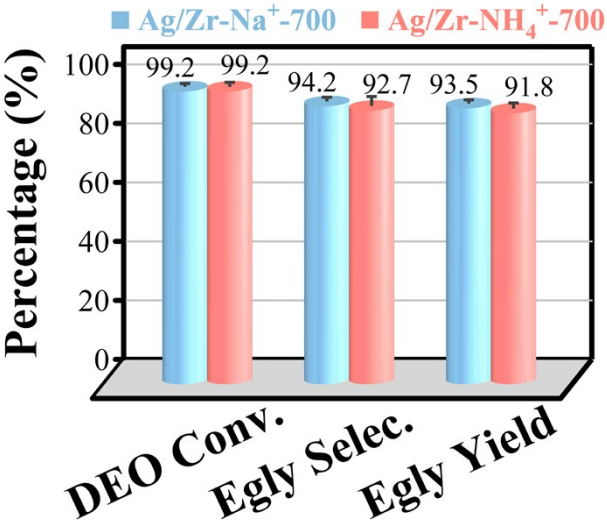

Fig. S11. Comparison of the activity of Ag/Zr-Na^+-700 and Ag/Zr-NH_4^+-700 catalysts.

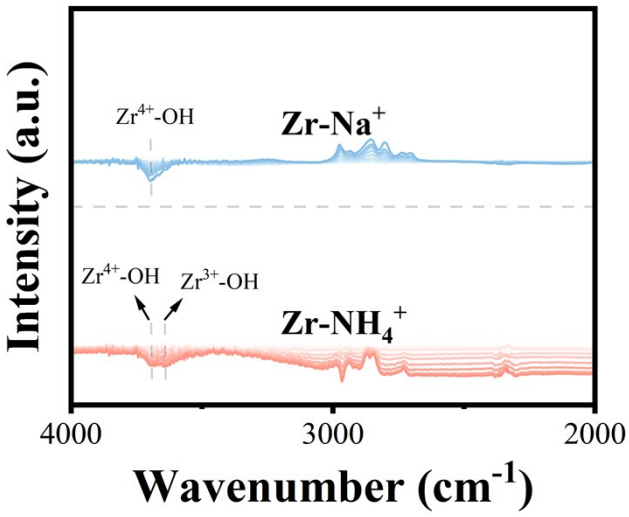

Fig. S12. In-situ adsorption FTIR of DEO on Zr-Na^+ and Zr-NH_4^+ catalysts.

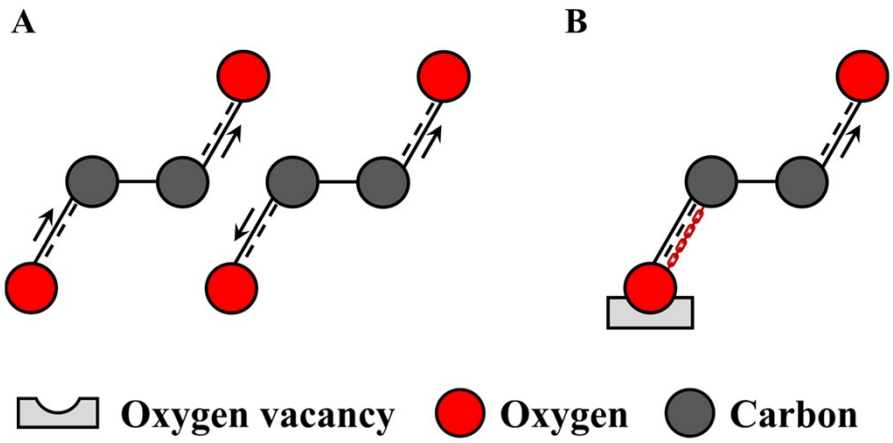

Fig. S13. Vibrational modelling of C=O bonds of DEO adsorbed on (A) Zr-Na^+ and (B) Zr-NH_4^+ catalysts.

The C=O bond pair adsorbed on Zr-Na^+ catalyst is free to vibrate, resulting in the coupling splitting into a pair of high-energy and low-energy states. Consequently, the infrared absorption peaks of the C=O bond exhibit a double peak. In contrast, one of the adsorbed C=O bond pairs on Zr-NH_4^+ catalyst is anchored, which results in the synchronisation of the C=O bond pair stretching, and thus its C=O bond infrared absorption peak is a single peak.

It is regrettable that we have not yet conducted a thorough investigation to substantiate this hypothesis. Consequently, it is only a reasonable supposition at this stage.

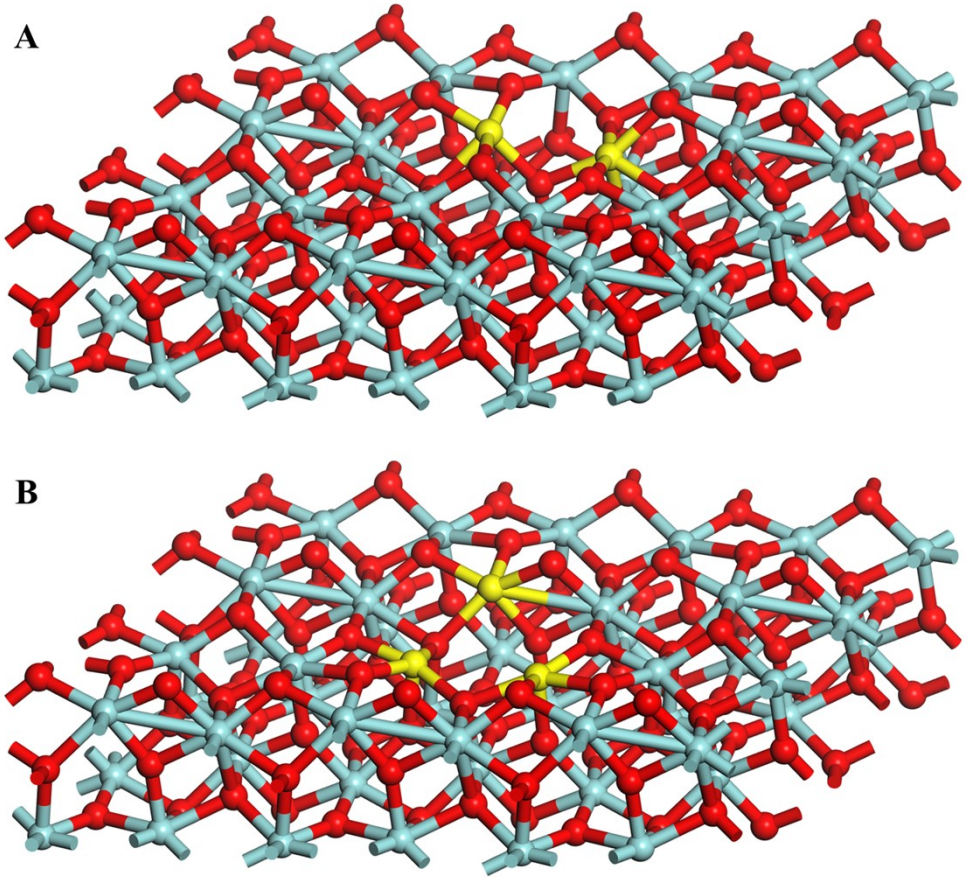

Fig. S14. (A) Two-coordinated and (B) three-coordinated oxygen vacancy on the (-111) crystalline plane of monoclinic zirconia (red for oxygen, cyan for zirconium, yellow for zirconium adjacent to the oxygen vacancies).

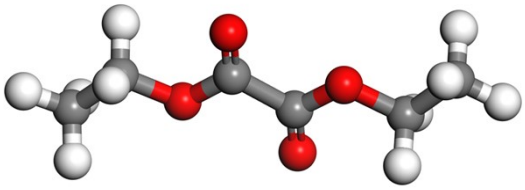

Fig. S15. The ball-and-stick model of DEO molecule (red for oxygen, dark grey for carbon, white for hydrogen).

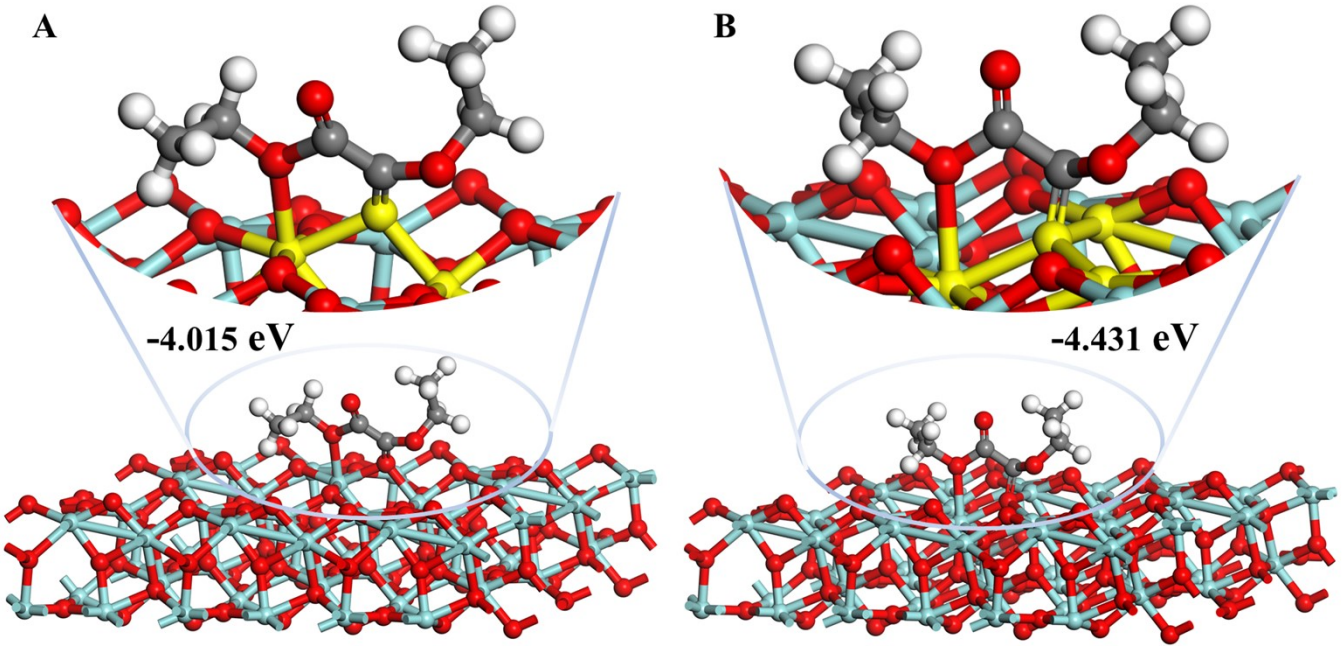

Fig. S16. DEO adsorption energies of (A) two- and (B) three-coordinated oxygen vacancies on (-111) crystalline plane of monoclinic zirconia (red for oxygen, cyan for zirconium, dark grey for carbon, white for hydrogen).

Reference

[1] G. Kresse, J. Furthmüller, Efficiency of ab-initio total energy calculations for metals and semiconductors using a plane-wave basis set, Computational Materials Science, 6 (1996) 15-50.

[2] J.P. Perdew, K. Burke, M. Ernzerhof, Generalized Gradient Approximation Made Simple, Phys Rev Lett, 77 (1996) 3865-3868.

[3] J.P. Perdew, J.A. Chevary, S.H. Vosko, K.A. Jackson, M.R. Pederson, D.J. Singh, C. Fiolhais, Atoms, molecules, solids, and surfaces: Applications of the generalized gradient approximation for exchange and correlation, Physical Review B, 46 (1992) 6671-6687.

[4] R. Ansari, M. Faghihnasiri, A. Shahnazari, S. Malakpour, S. Sahmani, A DFT study of thermal effects on the elastic properties of ZrO2 nanosheet, Journal of Alloys and Compounds, 687 (2016) 790-796.

[5] S. Grimme, J. Antony, S. Ehrlich, H. Krieg, A consistent and accurate ab initio parametrization of density functional dispersion correction (DFT-D) for the 94 elements H-Pu, The Journal of Chemical Physics, 132 (2010).

[6] A. Yin, X. Guo, W. Dai, K. Fan, High activity and selectivity of Ag/SiO2 catalyst for hydrogenation of dimethyl oxalate, Chemical Communications, 46 (2010) 4348-4350.

[7] A. Yin, C. Wen, W.-L. Dai, K. Fan, Ag/MCM-41 as a highly efficient mesostructured catalyst for the chemoselective synthesis of methyl glycolate and ethylene glycol, Applied Catalysis B-Environmental, 108 (2011) 90-99.

[8] J. Zheng, H. Lin, X. Zheng, X. Duan, Y. Yuan, Highly efficient mesostructured Ag/SBA-15 catalysts for the chemoselective synthesis of methyl glycolate by dimethyl oxalate hydrogenation, Catalysis Communications, 40 (2013) 129-133.

[9] J. Zhou, X. Duan, L. Ye, J. Zheng, M.M.-J. Li, S.E. Tsang, Y. Yuan, Enhanced chemoselective hydrogenation of dimethyl oxalate to methyl glycolate over bimetallic Ag–Ni/SBA-15 catalysts, Applied Catalysis A: General, 505 (2015) 344-353.

[10] J. Zheng, X. Duan, H. Lin, Z. Gu, H. Fang, J. Li, Y. Yuan, Silver nanoparticles confined in carbon nanotubes: on the understanding of the confinement effect and promotional catalysis for the selective hydrogenation of dimethyl oxalate, Nanoscale, 8 (2016) 5959-5967.

[11] M. Ouyang, Y. Wang, J. Zhang, Y. Zhao, S. Wang, X. Ma, Three dimensional Ag/KCC-1 catalyst with a hierarchical fibrous framework for the hydrogenation of dimethyl oxalate, RSC advances, 6 (2016) 12788-12791.

[12] M. Hu, Y. Yan, X. Duan, L. Ye, J. Zhou, H. Lin, Y. Yuan, Effective anchoring of silver nanoparticles onto N-doped carbon with enhanced catalytic performance for the hydrogenation of dimethyl oxalate to methyl glycolate, Catalysis Communications, 100 (2017) 148-152.

[13] X.Y. Cheng, Jun, Synthesis of methyl glycolate from the hydrogenation of dimethyl oxalate on Ag/SiO2 catalyst: the effects of Ag contents and promoters, Reaction kinetics,mechanisms and catalysis, 126 (2019).
[14] M. Ouyang, J. Wang, B. Peng, Y. Zhao, S. Wang, X. Ma, Effect of Ti on Ag catalyst supported on spherical fibrous silica for partial hydrogenation of dimethyl oxalate, Applied Surface Science, 466 (2019) 592-600.
[15] G. Dong, Y. Cao, S. Zheng, J. Zhou, W. Li, F. Zaera, X. Zhou, Catalyst consisting of Ag nanoparticles anchored on amine-derivatized mesoporous silica nanospheres for the selective hydrogenation of dimethyl oxalate to methyl glycolate, Journal of Catalysis, 391 (2020) 155-162.
[16] X.-p. Duan, T. Chen, T. Chen, L. Huang, L. Ye, B.T. Lo, Y. Yuan, S.C.E. Tsang, Intercalating lithium into the lattice of silver nanoparticles boosts catalytic hydrogenation of carbon–oxygen bonds, Chemical Science, 12 (2021) 8791-8802.
[17] Z. Luo, X. Xu, G. Dong, Y. Cao, S. Hu, G. Ye, Y.-A. Zhu, J. Zhou, W. Li, X. Zhou, Regulating mesopore structures of support toward enhanced selective hydrogenation of dimethyl oxalate to methyl glycolate on Ag catalysts, Chemical Engineering Journal, 450 (2022) 138397.
[18] S. Cheng, T. Meng, D. Mao, X. Guo, J. Yu, Selective Hydrogenation of Dimethyl Oxalate to Methyl Glycolate over Boron-Modified Ag/SiO2 Catalysts, Acs Omega, 7 (2022) 41224-41235.
[19] S. Cheng, T. Meng, D. Mao, X. Guo, J. Yu, Z. Ma, Ni-Modified Ag/SiO2 Catalysts for Selective Hydrogenation of Dimethyl Oxalate to Methyl Glycolate, Nanomaterials, 12 (2022).
[20] J. Zou, X. Duan, X. Liu, L. Huang, X. Liu, J. Zuo, W. Jiao, H. Lin, L. Ye, Y. Yuan, Identifying the activity origin of silver catalysts induced by interfacial electron localization for regioselective CO bond hydrogenation, Chemical Engineering Journal, 454 (2023) 140110.
[21] J. Ding, M.H. Fan, Q. Zhong, A.G. Russell, Single-atom silver-manganese nanocatalysts based on atom-economy design for reaction temperature-controlled selective hydrogenation of bioresources-derivable diethyl oxalate to ethyl glycolate and acetaldehyde diethyl acetal, Applied Catalysis B-Environmental, 232 (2018) 348-354.
[22] M. Guo, J. Ding, G. Ji, T. Xie, H. Pang, X. Li, Q. Zhong, Highly dispersed Ag/SiO2 catalyst with weak metal-support interaction for diethyl oxalate hydrogenation to ethyl glycolate, Molecular Catalysis, 556 (2024) 113898.